




# Potential improvement in power factor of $(\text{Bi}_{0.98}\text{Ge}_{0.02})_2\text{Te}_{2.7}\text{Se}_{0.3}$ compound due to defect engineering

Swaraangi Shirodkar<sup>1</sup>, A. N. Prabhu<sup>1,\*</sup> , Suchitra Putran<sup>1</sup>, Ashok Rao<sup>2</sup>, U. Deepika Shanubhogue<sup>2</sup>, and Ganesh Shridhar Hegde<sup>3,\*</sup>

<sup>1</sup> Department of Physics, Manipal Institute of Technology, Manipal Academy of Higher Education, Manipal 576104, India

<sup>2</sup> Centre for Clean Energy, Department of Physics, Manipal Institute of Technology, Manipal Academy of Higher Education, Manipal 576104, India

<sup>3</sup> Department of Physics, School of Applied Sciences, REVA University, Rukmini Knowledge Park, Yelahanka, Kattigenahalli, Bengaluru, Sathanur, Karnataka 560064, India

Received: 13 March 2024

Accepted: 23 April 2024

Published online:  
6 May 2024

© The Author(s), 2024

## ABSTRACT

In recent years, thermoelectricity has gained popularity as a renewable energy source, with applications including Peltier coolers and thermoelectric generators, particularly focusing on materials, like bismuth telluride and its doped derivatives. This study investigates  $\text{Bi}_2\text{Te}_3$ ,  $(\text{Bi}_{0.98}\text{Ge}_{0.02})_2\text{Te}_{2.7}\text{Se}_{0.3}$ , and  $(\text{Bi}_{0.98}\text{Ge}_{0.02})_2\text{Te}_{2.7}\text{Se}_{0.3}/\text{Bi}_2\text{Te}_3$  synthesized via solid-state reaction, revealing a rhombohedral structure in the XRD pattern and confirming chemical composition and composite homogeneity through EDS and porosity, density, and selenium integration via FESEM. Electrical resistivity decreases with rising temperature, while the Seebeck coefficient shows a linear increase, indicating n-type semiconductor behaviour. The highest power factor of  $108 \mu\text{W}/\text{mK}^2$  is achieved by  $(\text{Bi}_{0.98}\text{Ge}_{0.02})_2\text{Te}_{2.7}\text{Se}_{0.3}$ , contrasting with the lowest of  $20 \mu\text{W}/\text{mK}^2$  observed for the pristine sample at  $250^\circ\text{C}$ . Ge atoms enhance the power factor of  $(\text{Bi}_{0.98}\text{Ge}_{0.02})_2\text{Te}_{2.7}\text{Se}_{0.3}$  by 5.4 times compared to the pristine compound, making it ideal for thermoelectric applications through acceptor behaviour and defect engineering.

## 1 Introduction

Recently, thermoelectric materials have found increased demand for energy harvesting from wasted heat. They show important applications in power generation and coolers. Thermoelectric materials operate using the thermoelectric effect, which produces a

voltage in response to changes in temperature. This includes Seebeck and Peltier effects. The efficiency of thermoelectric material is given by power factor (PF) which can be expressed by

$$PF = \frac{S^2}{\rho} \quad (1)$$

Address correspondence to E-mail: ashwatha.prabhu@manipal.edu; ganeshhegde358@gmail.com

Here,  $S$  is the Seebeck coefficient, and  $\rho$  is the electrical resistivity [1]. Greater  $PF$  values results in a higher conversion efficiency. Therefore, lower the value of electrical resistivity will result in better conversion efficiency [2]. In semiconductors, achieving a high Seebeck coefficient necessitates a low carrier concentration, while maximizing electrical conductivity requires a high carrier concentration in metals. Furthermore, unlike metals, the carrier concentration has negligible impact on the electrical resistivity of doped semiconductors [3].

The insertion of germanium and selenium dopants into the lattice of  $\text{Bi}_2\text{Te}_3$  helped in optimisation of both thermal and electrical conductivity with the aid of defect engineering. By adding more phonon scattering centres and obstructing heat transfer through the material, selenium, on the other hand, helps lower thermal conductivity. By achieving the ideal balance between electrical and thermal conductivity, germanium and selenium when combined can enhance the thermoelectric performance of materials in a coordinated manner. A variety of applications in energy harvesting and waste heat recovery systems could benefit from the development of thermoelectric materials with improved efficiency in converting waste heat into electrical power, which is a promising project [4].

In a back-gate configuration, Mohammad Noorozi et al. [5] have demonstrated a physical model to characterize the thermoelectric materials of SiGe Nanowire. In nanowires, carrier transport was changed by biasing voltage to the gate at different temperatures. The power factor of SiGe nanowires was found to rise by more than two in the temperature range of 273 K to 450 K when compared to bulk SiGe. SiGe micro-thermoelectric generators ( $\mu\text{TEG}$ ) that harness daily waste heat show promise as an energy source. Si and SiGe nanowires are promising materials because of their low heat conductivity and strong electric conductivity. An extensive overview of Si and SiGe nanowires, including their fundamental thermoelectric principles, materials, architectures, production, and measurements, is given in the review by You et al. [6].

The most important class of thermoelectric materials is made up of  $\text{Bi}_2\text{Te}_3$  and  $\text{Bi}_2\text{Se}_3$  alloys because they exhibit the highest known thermoelectric efficiency at low and almost room temperatures. While alloys based on silicon are usually used in thermoelectric applications that need temperatures above 600 K [7]. The market for temperature control applications was recently dominated by  $\text{Bi}_2\text{Te}_3$  solid-state devices.

Peltier cooling systems, particularly the portable models, are gaining increased attention in response to the need to reduce the greenhouse gas effect because of their efficiency, which is on par with that of conventional refrigerant-based coolants [8, 9].

Sn's larger atomic mass and diameter affect thermal conductivity performance, with SiGe alloying causing a 40% reduction. Experimentally, phosphorous-doped  $\text{Ge}_{0.971}\text{Sn}_{0.029}$  NWs show higher electrical conductivity and Seebeck coefficient than Si and Ge NWs. However, high Sn content in SiSn alloy fabrication is challenging due to lattice mismatch and low solid solubility in Si [10, 11]. The thermal conductivity of SiGe NWs is affected by factors, such as Ge fraction, diameter ( $D$ ), and length. Thin NWs show a reduction in thermal conductivity compared to thick ones. The dependence on thermal conductivity becomes weaker with increasing  $D$  and Ge content. Longer NWs have a higher Seebeck coefficient, while thermal conductivity decreases with increased Ge concentration and NW length. N-type SiGe NWs have higher ZT and power factor compared to P-type NWs at 300 K, possibly due to temperature dependence of defect interaction [ref 6]. This work shows how to add 18% Sn content to GeSn layers using  $\text{SnCl}_4$  and  $\text{GeH}_4$  precursors, allow ingrain modulation, and enhance material quality, surface roughness, and optical properties [12–14].

We have synthesized bismuth telluride ( $\text{Bi}_2\text{Te}_3$ ) as a pristine,  $(\text{Bi}_{0.98}\text{Ge}_{0.02})_2\text{Te}_{2.7}\text{Se}_{0.3}$  and  $(\text{Bi}_{0.98}\text{Ge}_{0.02})_2\text{Te}_{2.7}\text{Se}_{0.3}/\text{Bi}_2\text{Te}_3$  composite structure in 5%, 10%, 15%, and 20% compositions via solid-state reaction. The prepared materials are exposed to the characterization methods such as Powder X-ray diffraction, Field Emission Scanning Electron Microscopy, Electrical Resistivity (30–250 °C), and Seebeck coefficient (30–250 °C). The research emphasizes the novelty of characterizing  $\text{Bi}_2\text{Te}_3$  doped with germanium using a variety of techniques, demonstrating a notable 5.4 times increase in power factor for  $(\text{Bi}_{0.98}\text{Ge}_{0.02})_2\text{Te}_{2.7}\text{Se}_{0.3}$ . This investigation shows intriguing applications in thermoelectric materials science and closes a knowledge gap for this combination of materials.

## 2 Experimental procedure

Solid-state reaction method was used for the synthesis of  $\text{Bi}_2\text{Te}_3$ ,  $(\text{Bi}_{0.98}\text{Ge}_{0.02})_2\text{Te}_{2.7}\text{Se}_{0.3}$ , and  $(\text{Bi}_{0.98}\text{Ge}_{0.02})_2\text{Te}_{2.7}\text{Se}_{0.3}/\text{Bi}_2\text{Te}_3$  for (95%/5%), (90%/10%),

(85%/15%), and (80%/20%) composites. The initial precursors used were bismuth (99.99%), germanium (99.9%), tellurium (99.99%), and selenium (99.995%), which were taken in stoichiometric ratios and sintered to get a polycrystalline sample as the final product.

### 2.1 a. Synthesis of $\text{Bi}_2\text{Te}_3$

Precursors such as bismuth and tellurium were taken in a stoichiometric ratio and then ground together for a homogeneous mixture in an agate mortar. The mixture was filled in a rectangular zig and formed into pellets with the use of a hydraulic press with 5 tons of pressure. The pellets were filled in a quartz tube that was then vacuum sealed. The pellets in the sealed ampoules were sintered in a tubular furnace for 24 h at 250 °C.

### 2.2 b. Synthesis of $(\text{Bi}_{0.98}\text{Ge}_{0.02})_2\text{Te}_{2.7}\text{Se}_{0.3}$

Precursors such as bismuth, tellurium, selenium, and germanium were taken in a stoichiometric ratio and then mixed in an agate mortar. 5 ton of pressure was used for the pelletization of the obtained homogeneous mixture which were then vacuum sealed in a quartz tube. The pellets were then sintered at 250 °C for 24 h.

### 2.3 c. Composition of $(\text{Bi}_{0.98}\text{Ge}_{0.02})_2\text{Te}_{2.7}\text{Se}_{0.3}/\text{Bi}_2\text{Te}_3$ for (95%/5%), (90%/10%), (85%/15%) and (80%/20%):

The  $\text{Bi}_2\text{Te}_3$  mixture was added to  $(\text{Bi}_{0.98}\text{Ge}_{0.02})_2\text{Te}_{2.7}\text{Se}_{0.3}$  in ratios of 5%, 10%, 15%, and 20% and was grounded for 1 h until a homogeneous mixture was obtained. The pellets were vacuum sealed and then sintered for 12 h.

### 2.4 d. Characterization

X-Ray Diffraction (XRD) was performed to find the crystallinity and purity of the compounds. X-Ray Diffractometer (Rigaku Miniflex) with  $\text{Cu } K\alpha$  rays (1.54 Å) was used in the  $2\theta$  range of 20° to 80°. Field Emission Scanning Electron Microscope (FESEM) and Energy-Dispersive X-ray Analysis of spectra (EDS) were performed using the instrument JEOL JSM-7100F to view the images of 50kx magnification at 10-kV voltage and to detect the presence of the elements in the sample, respectively. The temperature-dependent Seebeck

coefficient and electrical resistivity were measured using the instrument "Linesis LSR3" for the temperature range 30 °C to 250 °C.

## 3 Results and discussion

### 3.1 X-ray Diffraction (XRD)

XRD pattern for  $\text{Bi}_2\text{Te}_3$ ,  $(\text{Bi}_{0.98}\text{Ge}_{0.02})_2\text{Te}_{2.7}\text{Se}_{0.3}$  and  $(\text{Bi}_{0.98}\text{Ge}_{0.02})_2\text{Te}_{2.7}\text{Se}_{0.3}/\text{Bi}_2\text{Te}_3$  which have been observed to have rhombohedral crystal system with space group of  $R\bar{3}m$ . The XRD pattern (Fig. 1) matches with the JCPDS file (Fig. 3) (#08–0021). Using the Williamson–Hall formula, the crystallite size was measured (Refer Table 1). The crystallite size of the  $(\text{Bi}_{0.98}\text{Ge}_{0.02})_2\text{Te}_{2.7}\text{Se}_{0.3}$  sample is smaller than the base compound  $\text{Bi}_2\text{Te}_3$ , and  $(\text{Bi}_{0.98}\text{Ge}_{0.02})_2\text{Te}_{2.7}\text{Se}_{0.3}/\text{Bi}_2\text{Te}_3$  composite sample shows increased crystallite size from doped  $(\text{Bi}_{0.98}\text{Ge}_{0.02})_2\text{Te}_{2.7}\text{Se}_{0.3}$  compound and

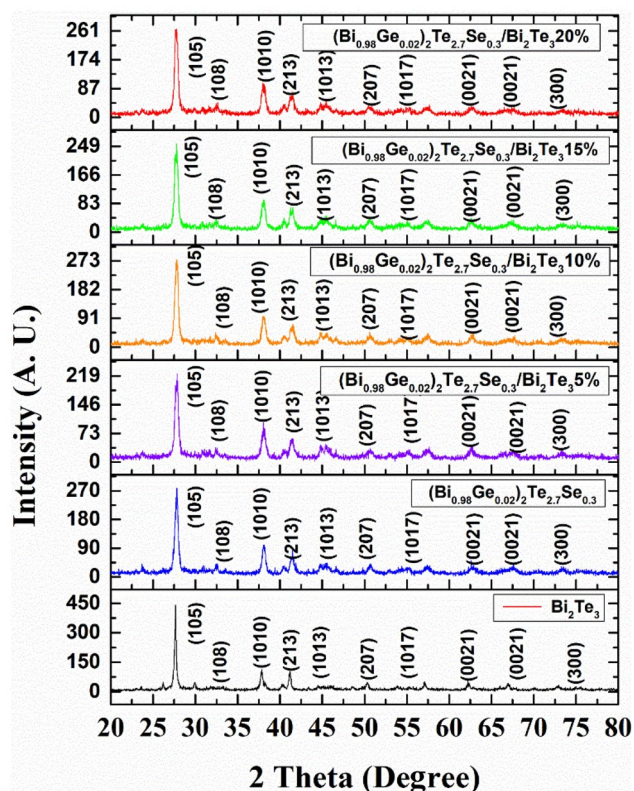


**Fig. 1** XRD peak pattern of (a)  $\text{Bi}_2\text{Te}_3$ , (b)  $(\text{Bi}_{0.98}\text{Ge}_{0.02})_2\text{Te}_{2.7}\text{Se}_{0.3}$ , (c)  $(\text{Bi}_{0.98}\text{Ge}_{0.02})_2\text{Te}_{2.7}\text{Se}_{0.3}/\text{Bi}_2\text{Te}_3$  5%, (d)  $(\text{Bi}_{0.98}\text{Ge}_{0.02})_2\text{Te}_{2.7}\text{Se}_{0.3}/\text{Bi}_2\text{Te}_3$  10%, (e)  $(\text{Bi}_{0.98}\text{Ge}_{0.02})_2\text{Te}_{2.7}\text{Se}_{0.3}/\text{Bi}_2\text{Te}_3$  15%, and (f)  $(\text{Bi}_{0.98}\text{Ge}_{0.02})_2\text{Te}_{2.7}\text{Se}_{0.3}/\text{Bi}_2\text{Te}_3$  20% composites

**Table 1** XRD data of  $(\text{Bi}_{1-x}\text{Ge}_x)_2\text{Te}_{2.7}\text{Se}_{0.3}/\text{Bi}_2\text{Te}_3$  composites

Sample	$R_p$	$R_{wp}$	$R_e$	$\chi^2$	Crystallite size (nm)	$a=b$ (Å)	$c$ (Å)	Lattice strain	Lorentz Factor	Defect Density $m^{-3}$
$\text{Bi}_2\text{Te}_3$	41.23	51.28	24.33	4.44	72.94	4.38	27.23	0.0017	0.892	16,082.67504
$(\text{Bi}_{1-x}\text{Ge}_x)_2\text{Te}_{2.7}\text{Se}_{0.3}$	39.72	49.70	23.01	4.66	33.07	4.36	28.09	0.0034	0.891	3645.554797
$(\text{Bi}_{1-x}\text{Ge}_x)_2\text{Te}_{2.7}\text{Se}_{0.3}/\text{Bi}_2\text{Te}_3$ 5%	39.01	49.32	23.54	4.38	60.26	4.34	29.69	0.0052	0.890	3359.646724
$(\text{Bi}_{1-x}\text{Ge}_x)_2\text{Te}_{2.7}\text{Se}_{0.3}/\text{Bi}_2\text{Te}_3$ 10%	40.77	50.56	22.84	4.89	77.43	4.41	27.38	0.0054	0.891	3168.980444
$(\text{Bi}_{1-x}\text{Ge}_x)_2\text{Te}_{2.7}\text{Se}_{0.3}/\text{Bi}_2\text{Te}_3$ 15%	37.19	46.43	23.39	3.93	27.55	4.15	29.31	0.0033	0.891	3231.739009
$(\text{Bi}_{1-x}\text{Ge}_x)_2\text{Te}_{2.7}\text{Se}_{0.3}/\text{Bi}_2\text{Te}_3$ 20%	38.92	48.87	22.83	4.58	31.71	4.18	28.34	0.0038	0.891	3194.07748

then again gradually decreases with an increase in the  $\text{Bi}_2\text{Te}_3$  content due to their defects. When point defects are concentrated enough, a diffuse scattering that resembles substitutional disorder occurs. Because of the elastic deformation of the lattice surrounding the defect, this happens because of the static displacement field. Point flaws, which can be introduced by material processing, are produced spontaneously by rising temperatures and can be quenched by cooling during sintering [15]. The increase in the crystallite size is due to the change in host and composite compound ratio which affects the crystallite size and its strain [16].

It has been observed that the highest peak of  $\text{Bi}_2\text{Te}_3$  coincides with the JCPDS file. As germanium and selenium are added, we can see that there is a shift in the most prominent peak to the higher  $2\theta$ . This is due to the substitution of Se atoms in tellurium sites. This substitution causes tensile stress in the lattice as the atomic radii of the two atoms are different [17]. Germanium atoms are also substituted in bismuth sites causing defects in the lattice.  $\text{Bi}_2\text{Te}_3$  usually crystallizes in hexagonal structure such as  $[\text{Te}-\text{Bi}-\text{Te}-\text{Bi}-\text{Te}]-[\text{Te}-\text{Bi}-\text{Te}-\text{Bi}-\text{Te}]$  bonded by Van der Waals force. When dopants such as Ge and Se are added, it substitutes bismuth and tellurium interstitially within a quintuple layer and the stacking of  $[-\text{BiGe}-\text{TeSe}-\text{BiGe}-\text{TeSe}-]$  takes place [18]. When the crystallographic orientation does not change, antiphase barriers form and an opposing phase develops on both sides of the boundary: For instance, by stopping the stacking sequence, a crystal order  $\text{Se}-\text{Bi}-\text{Te}-\text{Sn}-\text{Te}-\text{Bi}-\text{Se}$  might have an antiphase border [15]. One possibility for defect engineering of  $\text{Bi}_2\text{Te}_3$  is that some of the Sn atoms are incorporated into the

lattice, resulting in a seven-layered lamellar structure,  $\text{Te}-\text{Bi}-\text{Te}-\text{Sn}-\text{Te}-\text{Bi}-\text{Te}$ . If a similar structure exists in Sn-doped BTS, it will be  $\text{Se}-\text{Bi}-\text{Te}-\text{Sn}-\text{Te}-\text{Bi}-\text{Se}$ . It is important to note that, unlike those occupying the Bi site, the Sn atoms in this structure do not contribute any charge to the lattice, hence the disparity is resolved. However, no further diffraction peaks are visible, except for those corresponding to the chalcogen-ordered tetradymite structure in the XRD [19]. As an additional analysis XRD the defect density ( $D$ ) and Lorentz Factor ( $p$ ) are calculated using

$$D = \frac{K_\alpha}{4.36b^2}, \quad (2)$$

$$p = \frac{1 + \cos^2 2\theta}{2}, \quad (3)$$

where  $K_\alpha$  is 0.9 and  $b$  is the Full width half maximum intensity (FWHM) [15],

For the composite samples, as bismuth telluride is added in proportion to  $(\text{Bi}_{0.98}\text{Ge}_{0.02})_2\text{Te}_{2.7}\text{Se}_{0.3}$ , the prominent peak starts shifting (Fig. 2) to the lower  $2\theta$  indicating the increase of  $\text{Bi}_2\text{Te}_3$  lattices. Negatively charged Ge impurity in the range of low concentrations enter the van der Waals gap of Bi and Te crystal lattice where they form a new atomic plane periodically repeated in the direction of the trigonal  $c$ -axis of the crystal. The JCPDS file for bismuth telluride is shown in Fig. 3. There can be seen a gradual peak broadening from pristine  $\text{Bi}_2\text{Te}_3$  to  $(\text{Bi}_{0.98}\text{Ge}_{0.02})_2\text{Te}_{2.7}\text{Se}_{0.3}/\text{Bi}_2\text{Te}_3$  20%. This is due to the defects present in the crystal. Bismuth telluride is anisotropic in nature and has good periodicity hence can be seen as possessing high intensity and

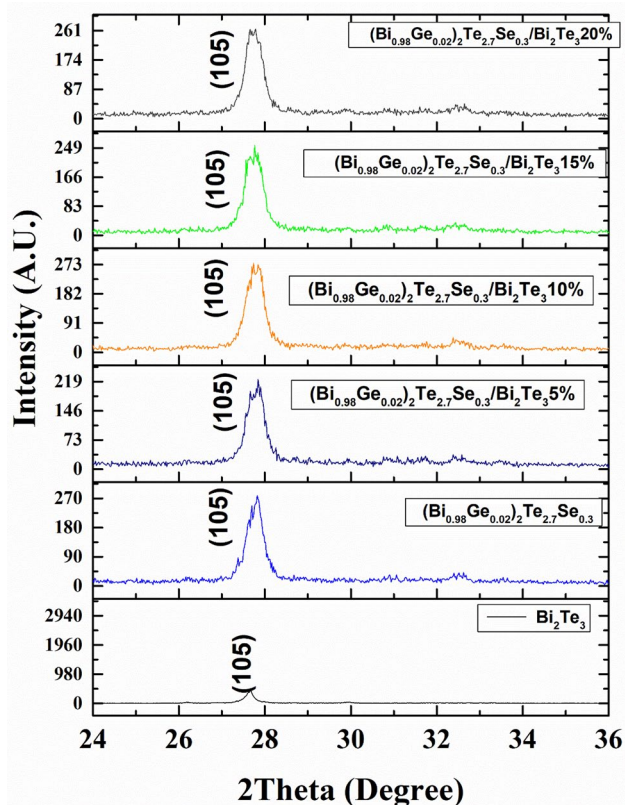


**Fig. 2** Shifting in XRD peak pattern of (a)  $\text{Bi}_2\text{Te}_3$ , (b)  $(\text{Bi}_{0.98}\text{Ge}_{0.02})_2\text{Te}_{2.7}\text{Se}_{0.3}$ , (c)  $(\text{Bi}_{0.98}\text{Ge}_{0.02})_2\text{Te}_{2.7}\text{Se}_{0.3} / \text{Bi}_2\text{Te}_3$  5%, (d)  $(\text{Bi}_{0.98}\text{Ge}_{0.02})_2\text{Te}_{2.7}\text{Se}_{0.3} / \text{Bi}_2\text{Te}_3$  10%, (e)  $(\text{Bi}_{0.98}\text{Ge}_{0.02})_2\text{Te}_{2.7}\text{Se}_{0.3} / \text{Bi}_2\text{Te}_3$  15%, and (f)  $(\text{Bi}_{0.98}\text{Ge}_{0.02})_2\text{Te}_{2.7}\text{Se}_{0.3} / \text{Bi}_2\text{Te}_3$  20% composites

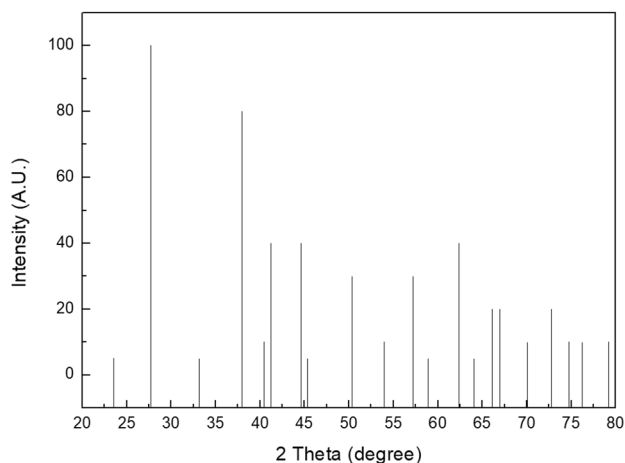


**Fig. 3** JCPDS file for bismuth telluride

the composites can be seen as having higher intensity compared to  $(\text{Bi}_{0.98}\text{Ge}_{0.02})_2\text{Te}_{2.7}\text{Se}_{0.3}$  sample [20]. Rietveld refinement software EXPO 2014 was used which

gives the difference in the theoretical and observed peak patterns in XRD. Table 1 gives the values of  $R_p$ ,  $R_{wp}$ ,  $R_e$  and  $\chi^2$  and are shown in Fig. 4.

### 3.2 Field Emission Scanning Electron Microscopy (FESEM)

FESEM characterization was carried out at 50kx magnification in order to comprehend the morphology on the pellets' surface, as indicated in Fig. 5. The surface of Bismuth telluride, seen in Fig. 5a, has a rough surface and an uneven configuration. Bismuth telluride doped with germanium and selenium is shown in Fig. 5b. This has larger grain boundaries and reduced porosity. The composites are displayed in Figs. 5c–f. As the doped compound's bismuth telluride content rises, porosity also begins to rise. This suggests that the interstitial sites have absorbed the selenium [21]. When the sintering temperature was raised to almost  $250^\circ\text{C}$ , some pores grew to the size of  $\sim 10\text{ nm}$  and the number of these large pores increased with raising annealing temperature, in addition to some smaller pores. Compared to tellurium since selenium has a much higher vaporization pressure [22]. This feature of selenium atoms leads to the formation of donor-like voids in the bismuth telluride lattice. More porosity patches are created during sintering because of the selenium atoms vaporizing since there are more Te sites for them to occupy. This demonstrates that the polycrystalline grains in the sample's localized  $(\text{Bi}_{0.98}\text{Ge}_{0.02})_2\text{Te}_{2.7}\text{Se}_{0.3} / \text{Bi}_2\text{Te}_3$  20%-layered crystallites. Additionally, it demonstrates that Ge is evenly distributed across the sample and that no evidence of an independent Ge or GeTe cluster has been found [21].

### 3.3 Energy-dispersive spectra analysis of X-ray (EDS)

The chemical composition of the samples and the materials added to them were investigated. Tellurium and bismuth are displayed in Fig. 6a, while germanium and selenium are displayed alongside with bismuth and tellurium in Fig. 6b. Figures 6c–f shows each element that was added to each composite, including tellurium, germanium, bismuth, and selenium. Based on our analysis of the germanium content analysis using the energy-dispersive analyser, we believe that the following impact further supports the stated conclusion on the nature of incorporation of Ge atoms into the crystal lattice of

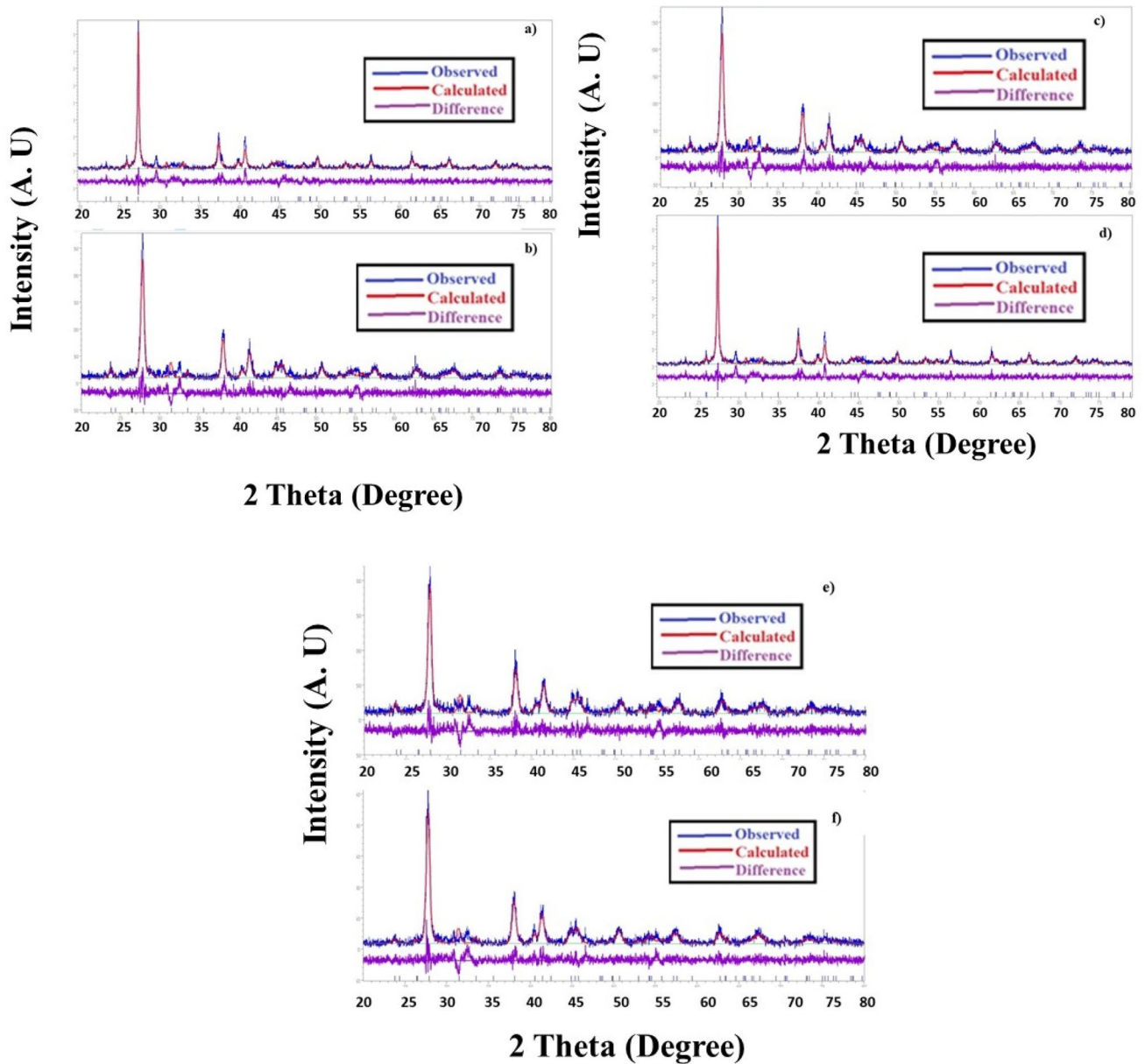


**Fig. 4** Rietveld Refinement plots for XRD peak pattern of (a)  $(\text{Bi}_2\text{Te}_3)$ , (b)  $(\text{Bi}_{0.98}\text{Ge}_{0.02})_2\text{Te}_{2.7}\text{Se}_{0.3}$ , (c)  $(\text{Bi}_{0.98}\text{Ge}_{0.02})_2\text{Te}_{2.7}\text{Se}_{0.3} / \text{Bi}_2\text{Te}_3$  5%, (d)  $(\text{Bi}_{0.98}\text{Ge}_{0.02})_2\text{Te}_{2.7}\text{Se}_{0.3} / \text{Bi}_2\text{Te}_3$  10%, (e)  $(\text{Bi}_{0.98}\text{Ge}_{0.02})_2\text{Te}_{2.7}\text{Se}_{0.3} / \text{Bi}_2\text{Te}_3$  15%, and (f)  $(\text{Bi}_{0.98}\text{Ge}_{0.02})_2\text{Te}_{2.7}\text{Se}_{0.3} / \text{Bi}_2\text{Te}_3$  20% composites

Bi and Te. All of the samples under investigation had energy spectra collected from their natural cleavage faces, and these spectra were limited to the bands of distinctive X-ray radiation from Te and Bi (refer to Fig. 6a). This observation could lead that all the germanium added to the host is segregated, that is,

there is less germanium integrated in to the Bi and Te lattice than the detected limit.

### 3.4 Electrical resistivity

Electrical resistivity of the prepared samples were measured in the temperature range 30 °C to 250 °C

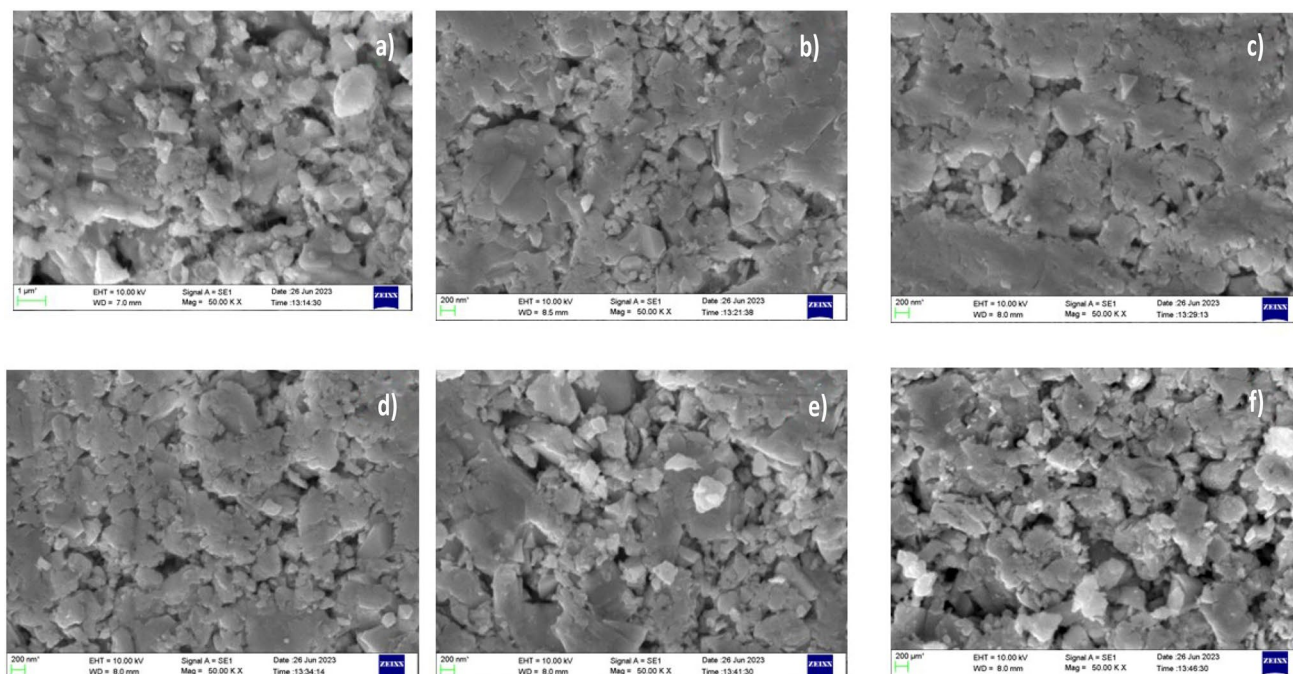


**Fig. 5** Surface morphological features of (a)  $\text{Bi}_2\text{Te}_3$ , (b)  $(\text{Bi}_{0.98}\text{Ge}_{0.02})_2\text{Te}_{2.7}\text{Se}_{0.3}$ , (c)  $(\text{Bi}_{0.98}\text{Ge}_{0.02})_2\text{Te}_{2.7}\text{Se}_{0.3} / \text{Bi}_2\text{Te}_3$  5%, (d)  $(\text{Bi}_{0.98}\text{Ge}_{0.02})_2\text{Te}_{2.7}\text{Se}_{0.3} / \text{Bi}_2\text{Te}_3$  10%, (e)  $(\text{Bi}_{0.98}\text{Ge}_{0.02})_2\text{Te}_{2.7}\text{Se}_{0.3} / \text{Bi}_2\text{Te}_3$  15%, and (f)  $(\text{Bi}_{0.98}\text{Ge}_{0.02})_2\text{Te}_{2.7}\text{Se}_{0.3} / \text{Bi}_2\text{Te}_3$  20% composites

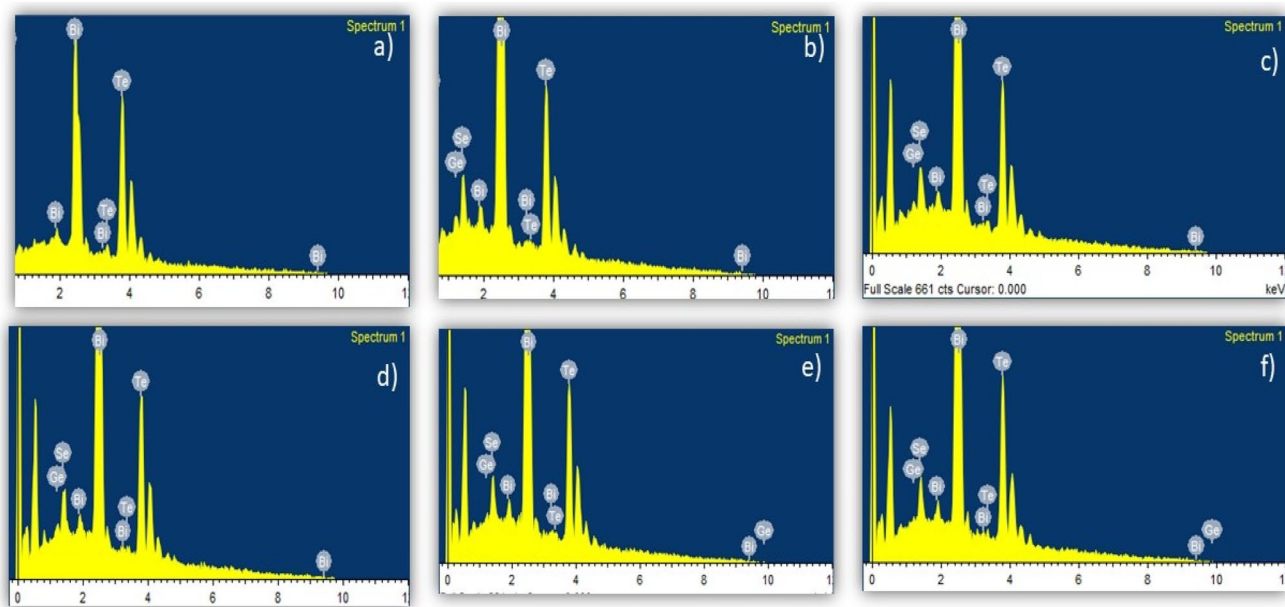


**Fig. 6** Elemental composition images (EDS) of (a)  $\text{Bi}_2\text{Te}_3$ , (b)  $(\text{Bi}_{0.98}\text{Ge}_{0.02})_2\text{Te}_{2.7}\text{Se}_{0.3}$ , (c)  $(\text{Bi}_{0.98}\text{Ge}_{0.02})_2\text{Te}_{2.7}\text{Se}_{0.3} / \text{Bi}_2\text{Te}_3$  5%, (d)  $(\text{Bi}_{0.98}\text{Ge}_{0.02})_2\text{Te}_{2.7}\text{Se}_{0.3} / \text{Bi}_2\text{Te}_3$  10%, (e)  $(\text{Bi}_{0.98}\text{Ge}_{0.02})_2\text{Te}_{2.7}\text{Se}_{0.3} / \text{Bi}_2\text{Te}_3$  15%, and (f)  $(\text{Bi}_{0.98}\text{Ge}_{0.02})_2\text{Te}_{2.7}\text{Se}_{0.3} / \text{Bi}_2\text{Te}_3$  20% composites

(Fig. 7). All samples exhibit a decrease in electrical resistivity with increasing temperature. This demonstrates the semiconducting behaviour of the samples

over the entire temperature range. The Bi atoms in the  $\text{Bi}_2\text{Te}_3$  structure coordinate with six Te atoms to form different lattice vacancies. The addition of

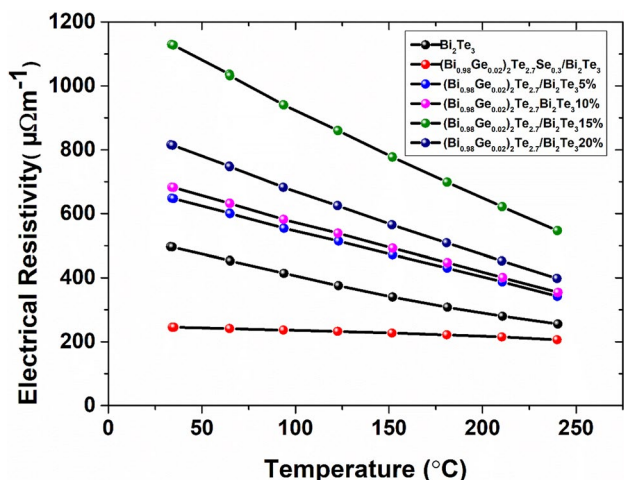


**Fig. 7** Temperature-dependent electrical resistivity of (a)  $\text{Bi}_2\text{Te}_3$ , (b)  $(\text{Bi}_{0.98}\text{Ge}_{0.02})_2\text{Te}_{2.7}\text{Se}_{0.3}$ , (c)  $(\text{Bi}_{0.98}\text{Ge}_{0.02})_2\text{Te}_{2.7}\text{Se}_{0.3}/\text{Bi}_2\text{Te}_3$  5%, (d)  $(\text{Bi}_{0.98}\text{Ge}_{0.02})_2\text{Te}_{2.7}\text{Se}_{0.3}/\text{Bi}_2\text{Te}_3$  10%, (e)  $(\text{Bi}_{0.98}\text{Ge}_{0.02})_2\text{Te}_{2.7}\text{Se}_{0.3}/\text{Bi}_2\text{Te}_3$  15%, and (f)  $(\text{Bi}_{0.98}\text{Ge}_{0.02})_2\text{Te}_{2.7}\text{Se}_{0.3}/\text{Bi}_2\text{Te}_3$  20% composites

germanium and selenium to the compound fills in the voids. While there is also coordination between Ge with Te and Ge with Se, some of the Bi is also coordinated with Ge and Te is coordinated with Se. Two crucial elements in determining the bulk of charge carriers, carrier concentration, and transport characteristics in  $\text{Bi}_2\text{Te}_3$ -based materials are the anion vacancies and anti-site defects engineering [23]. Tellurium  $\text{Te}_{(1)}$  and  $\text{Te}_{(2)}$  have two crystallographic sites, resulting in anti-structure defects, such as  $\text{Bi-Ge-Te}_{(1)}$  and  $\text{Bi-Ge-Te}_{(2)}$ . The decrease in electrical resistivity with an increase in temperature is due to the reduction of the Te vacancies after the doping of Ge. The stoichiometry of the bismuth in  $\text{Bi}_2\text{Te}_3$  is altered by the addition of germanium to the sublattices of tellurium and selenium. Due of the reduced lattice vibration of germanium,  $\text{Bi}_2\text{Te}_3$  is more stable at higher temperatures. The sintering process forms anti-site defects of  $\text{BiTe}$ ,  $\text{GeTe}$ ,  $\text{BiSe}$ , and  $\text{GeSe}$ . These flaws also contribute to the negative trending behaviour of electrical resistivity [24].

The concentration of free carriers rises in the  $\text{Bi}_2\text{Te}_3$  lattice when Ge impurity atoms are present. It is observed that Ge atom acts as acceptor in the  $\text{Bi}_2\text{Te}_3$  lattice through the substitution of Se on Te atoms, hence the insertion of Ge into the Bi cation sublattice leads to occupation of Ge atoms in Van der Waals sites of the Bi atom. The high density

of grain boundary defects in composite structures causes the carriers scattering behaviour, resulting in the decrease in the electrical resistivity [25]. At high density of 20%  $\text{Bi}_2\text{Te}_3$  embedded in the composite, distance between the particles reduces which is found to be an unpredicted phenomenon. These behaviour leads to the increase of scattered electrons, resulting in random variation in the electrical resistivity [26, 27].

### 3.5 Linear fitting of SPH model

The linear plot of  $\ln(\rho/T)$  and  $1/T$  in Fig. 8 shows that the hopping mechanism between nearest

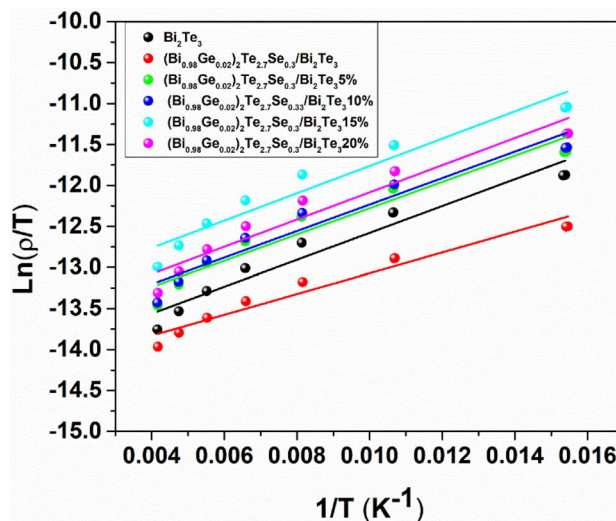


**Fig. 8** Linear Fitting of SPH model of a)  $\text{Bi}_2\text{Te}_3$ , b)  $(\text{Bi}_{0.98}\text{Ge}_{0.02})_2\text{Te}_{2.7}\text{Se}_{0.3}$ , c)  $(\text{Bi}_{0.98}\text{Ge}_{0.02})_2\text{Te}_{2.7}\text{Se}_{0.3}/\text{Bi}_2\text{Te}_3$  5%, d)  $(\text{Bi}_{0.98}\text{Ge}_{0.02})_2\text{Te}_{2.7}\text{Se}_{0.3}/\text{Bi}_2\text{Te}_3$  10%, e)  $(\text{Bi}_{0.98}\text{Ge}_{0.02})_2\text{Te}_{2.7}\text{Se}_{0.3}/\text{Bi}_2\text{Te}_3$  15%, and f)  $(\text{Bi}_{0.98}\text{Ge}_{0.02})_2\text{Te}_{2.7}\text{Se}_{0.3}/\text{Bi}_2\text{Te}_3$  20% composites

**Table 2** Activation energy of  $\text{Bi}_2\text{Te}_3$ , b)  $(\text{Bi}_{1-x}\text{Ge}_x)_2\text{Te}_{2.7}\text{Se}_{0.3}$ , c)  $(\text{Bi}_{1-x}\text{Ge}_x)_2\text{Te}_{2.7}\text{Se}_{0.3}/\text{Bi}_2\text{Te}_3$  5%, d)  $(\text{Bi}_{1-x}\text{Ge}_x)_2\text{Te}_{2.7}\text{Se}_{0.3}/\text{Bi}_2\text{Te}_3$  10%, e)  $(\text{Bi}_{1-x}\text{Ge}_x)_2\text{Te}_{2.7}\text{Se}_{0.3}/\text{Bi}_2\text{Te}_3$  15%, and f)  $(\text{Bi}_{1-x}\text{Ge}_x)_2\text{Te}_{2.7}\text{Se}_{0.3}/\text{Bi}_2\text{Te}_3$  20% composites

Sample	$E_A$ (meV)
$\text{Bi}_2\text{Te}_3$	12.0
$(\text{Bi}_{1-x}\text{Ge}_x)_2\text{Te}_{2.7}\text{Se}_{0.3}$	10.0
$(\text{Bi}_{1-x}\text{Ge}_x)_2\text{Te}_{2.7}\text{Se}_{0.3}/\text{Bi}_2\text{Te}_3$ 5%	13.6
$(\text{Bi}_{1-x}\text{Ge}_x)_2\text{Te}_{2.7}\text{Se}_{0.3}/\text{Bi}_2\text{Te}_3$ 10%	13.7
$(\text{Bi}_{1-x}\text{Ge}_x)_2\text{Te}_{2.7}\text{Se}_{0.3}/\text{Bi}_2\text{Te}_3$ 15%	13.8
$(\text{Bi}_{1-x}\text{Ge}_x)_2\text{Te}_{2.7}\text{Se}_{0.3}/\text{Bi}_2\text{Te}_3$ 20%	14.3



adjacent sites is formed by thermally activated tiny polarons in  $(\text{Bi}_2\text{Te}_3)$ ,  $(\text{Bi}_{0.98}\text{Ge}_{0.02})_2\text{Te}_{2.7}\text{Se}_{0.3}$ , and  $(\text{Bi}_{0.98}\text{Ge}_{0.02})_2\text{Te}_{2.7}\text{Se}_{0.3}/\text{Bi}_2\text{Te}_3$  (5%, 10%, 15%, and 20% compositions) system. The composition of selenium atoms may change during sintering, resulting in EA values (Table 2) that fluctuate inconsistently with doping concentration [28].

At increasing Ge doping concentrations, the wave functions of the Ge acceptors overlap substantially, forming an impurity band. Increasing Ge concentration causes a rise in the impurity band's density of states (DOS) rather than hole doping. The impurity band in all samples was found to be 12 to 15 meV below the top of the upper valence band [29]. However, in the case of Ge-doped  $\text{Bi}_2\text{Te}_3$ , this Sn-related impurity band is most likely located within the bulk band gap, because the activation energy was found to be 20% higher in  $(\text{Bi}_{1-x}\text{Ge}_x)_2\text{Te}_{2.7}\text{Se}_{0.3}/\text{Bi}_2\text{Te}_3$  than any other composite, implying the appearance of a new impurity band to pin the chemical potential in Ge-doped  $\text{Bi}_2\text{Te}_3$ . It should be noted that in Ge-doped  $\text{Bi}_2\text{Te}_3$ , there may be an impurity band caused by Se vacancies and extra  $\text{Bi}_2\text{Te}_3$  anti-site defects. Due to its high DOS,  $E_F$  is most likely anchored to the Ge-related impurity band. As a result, the activation energy  $E_a$  varies practically at random [30, 31].

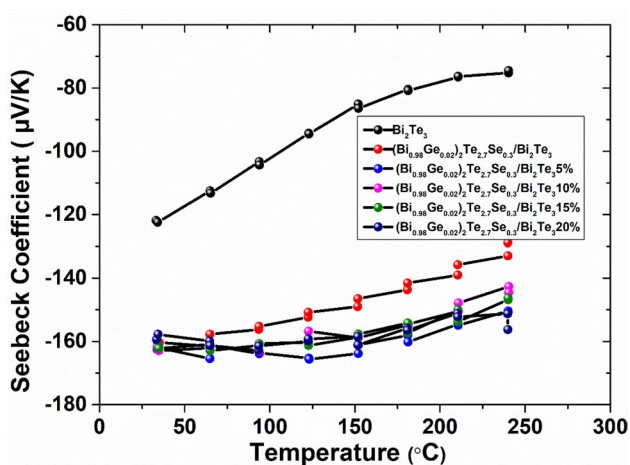


**Fig. 9** Temperature vs Seebeck Coefficient of (a)  $\text{Bi}_2\text{Te}_3$ , (b)  $(\text{Bi}_{0.98}\text{Ge}_{0.02})_2\text{Te}_{2.7}\text{Se}_{0.3}$ , (c)  $(\text{Bi}_{0.98}\text{Ge}_{0.02})_2\text{Te}_{2.7}\text{Se}_{0.3} / \text{Bi}_2\text{Te}_3$  5%, (d)  $(\text{Bi}_{0.98}\text{Ge}_{0.02})_2\text{Te}_{2.7}\text{Se}_{0.3} / \text{Bi}_2\text{Te}_3$  10%, (e)  $(\text{Bi}_{0.98}\text{Ge}_{0.02})_2\text{Te}_{2.7}\text{Se}_{0.3} / \text{Bi}_2\text{Te}_3$  15%, and (f)  $(\text{Bi}_{0.98}\text{Ge}_{0.02})_2\text{Te}_{2.7}\text{Se}_{0.3} / \text{Bi}_2\text{Te}_3$  20% composites

### 3.6 Seebeck Coefficient and Power Factor

Seebeck coefficient was measured in the temperature range of 30–250 °C. The negative values of Seebeck coefficient shown in Fig. 9 illustrates the *n*-type semiconducting behaviour of all the samples. The majority of charge carriers in the *n*-type material are electrons. It shows how, even at temperatures as high as 250 °C, all samples stay in the *n*-type area despite the Seebeck coefficient increasing linearly with temperature. The anti-site defect engineering produced in the samples determine the carrier concentration. The electrical conductivity and Seebeck coefficient are unintentionally impacted by this [32]. The Seebeck coefficient is enhanced by the lattice defect. It moves the donor band closer to the conduction band. More electrons are liberated in the conduction band because of the flaws in the lattices caused by the insertion of Se and Ge, increasing the flow of electrons [33].

At 122 °C, the composite sample  $(\text{Bi}_{0.98}\text{Ge}_{0.02})_2\text{Te}_{2.7}\text{Se}_{0.3} / \text{Bi}_2\text{Te}_3$  has the highest Seebeck coefficient, measuring 165.4  $\mu\text{V}/\text{K}$ . Also, it is evident that when the temperature rises, the sample loses electrons, which results in a decrease in the carrier concentration of the majority charge carriers and an increase in the formation of holes. The Ge atoms' acceptor-like behaviour is most likely caused by their integration into the Bi sublattice, where they give rise to negatively charged GeBi substitutional defects [34, 35]. Because holes balance the charge of GeBi substitutional defects, the concentration of free charge carriers rises. The remaining Ge atoms are integrated without changing the hole concentration. Adopting the notion that Ge atoms in the van der Waals gap form seven-layer lamellae seems reasonable. The charge transfer causes band bending at the metal–semiconductor contact, which is characterized by an electrical potential difference. This activity creates an energy-dependent barrier that works as a filter, scattering low-energy electrons. As a result, we discovered that the Seebeck coefficient varies randomly with doping [36]. The values of theoretical carrier concentrations, mobility, and scattering factor are given in Table 3. However, the impurity level's influence on the material's Seebeck coefficient weakens when the Ge content rises higher and the Fermi level moves away from the impurity level's location. As the carrier concentration rises more, the Seebeck coefficient falls [37].

$\text{Bi}_2\text{Te}_3$ ,  $(\text{Bi}_{0.98}\text{Ge}_{0.02})_2\text{Te}_{2.7}\text{Se}_{0.3} / \text{Bi}_2\text{Te}_3$ , and  $(\text{Bi}_{0.98}\text{Ge}_{0.02})_2\text{Te}_{2.7}\text{Se}_{0.3} / \text{Bi}_2\text{Te}_3$  composites were power

**Table 3** Theoretical carrier concentrations, mobility and scattering factor of a)  $\text{Bi}_2\text{Te}_3$ , b)  $(\text{Bi}_{0.98}\text{Ge}_{0.02})_2\text{Te}_{2.7}\text{Se}_{0.3}$ , c)  $(\text{Bi}_{0.98}\text{Ge}_{0.02})_2\text{Te}_{2.7}\text{Se}_{0.3} / \text{Bi}_2\text{Te}_3$  5%, d)  $(\text{Bi}_{0.98}\text{Ge}_{0.02})_2\text{Te}_{2.7}\text{Se}_{0.3} / \text{Bi}_2\text{Te}_3$  10% e)  $(\text{Bi}_{0.98}\text{Ge}_{0.02})_2\text{Te}_{2.7}\text{Se}_{0.3} / \text{Bi}_2\text{Te}_3$  15%, and f)  $(\text{Bi}_{0.98}\text{Ge}_{0.02})_2\text{Te}_{2.7}\text{Se}_{0.3} / \text{Bi}_2\text{Te}_3$  20% composites

Sample	$n_{\text{Th}}$ $10^{27}(\text{m}^{-3})$	$\mu_{\text{Th}}$ $10^{-4}$ $(\text{m}^2/\text{Vs})$	$\gamma_{\text{Th}}$
$\text{Bi}_2\text{Te}_3$	1.7	0.14	62.70
$(\text{Bi}_{0.98}\text{Ge}_{0.02})_2\text{Te}_{2.7}\text{Se}_{0.3}$	0.7	0.4	61.81
$(\text{Bi}_{0.98}\text{Ge}_{0.02})_2\text{Te}_{2.7}\text{Se}_{0.3} / \text{Bi}_2\text{Te}_3$ 5%	0.5	0.3	61.47
$(\text{Bi}_{0.98}\text{Ge}_{0.02})_2\text{Te}_{2.7}\text{Se}_{0.3} / \text{Bi}_2\text{Te}_3$ 10%	2.7	0.06	63.16
$(\text{Bi}_{0.98}\text{Ge}_{0.02})_2\text{Te}_{2.7}\text{Se}_{0.3} / \text{Bi}_2\text{Te}_3$ 15%	0.6	0.19	61.60
$(\text{Bi}_{0.98}\text{Ge}_{0.02})_2\text{Te}_{2.7}\text{Se}_{0.3} / \text{Bi}_2\text{Te}_3$ 20%	0.5	0.31	61.47

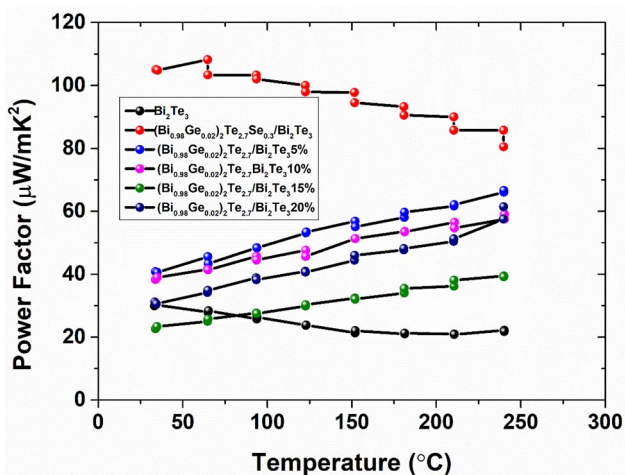


**Fig. 10** Temperature-dependent power factor of (a)  $\text{Bi}_2\text{Te}_3$ , (b)  $(\text{Bi}_{0.98}\text{Ge}_{0.02})_2\text{Te}_{2.7}\text{Se}_{0.3}$ , (c)  $(\text{Bi}_{0.98}\text{Ge}_{0.02})_2\text{Te}_{2.7}\text{Se}_{0.3} / \text{Bi}_2\text{Te}_3$  5%, (d)  $(\text{Bi}_{0.98}\text{Ge}_{0.02})_2\text{Te}_{2.7}\text{Se}_{0.3} / \text{Bi}_2\text{Te}_3$  10%, (e)  $(\text{Bi}_{0.98}\text{Ge}_{0.02})_2\text{Te}_{2.7}\text{Se}_{0.3} / \text{Bi}_2\text{Te}_3$  15%, and (f)  $(\text{Bi}_{0.98}\text{Ge}_{0.02})_2\text{Te}_{2.7}\text{Se}_{0.3} / \text{Bi}_2\text{Te}_3$  20% composites

factor analysed throughout a temperature range of 30–250 °C (Fig. 10).  $(\text{Bi}_{0.98}\text{Ge}_{0.02})_2\text{Te}_{2.7}\text{Se}_{0.3}$  has the highest power factor of  $108 \mu\text{W}/\text{mK}^2$  and the lowest  $20 \mu\text{W}/\text{mK}^2$  is obtained by pristine at 250 °C. The dramatic positive variation from composite to pure is related to simultaneous changes in Seebeck coefficient and electrical resistivity. As a result,  $(\text{Bi}_{0.98}\text{Ge}_{0.02})_2\text{Te}_{2.7}\text{Se}_{0.3}$  has a power factor value that is approximately 5.4 times higher than that of the pristine. Based on the data presented above, we can conclude that the doped material  $(\text{Bi}_{0.98}\text{Ge}_{0.02})_2\text{Te}_{2.7}\text{Se}_{0.3}$  performs substantially better than virgin  $\text{Bi}_2\text{Te}_3$  and other composites. The result of the present work is compared with the others in Table 4 [38–40].

### 4 Conclusion

In the present work, bismuth telluride was synthesized in various compositions, including pristine,  $(\text{Bi}_{0.98}\text{Ge}_{0.02})_2\text{Te}_{2.7}\text{Se}_{0.3}$ , and  $(\text{Bi}_{0.98}\text{Ge}_{0.02})_2\text{Te}_{2.7}\text{Se}_{0.3} / \text{Bi}_2\text{Te}_3$ . The materials were characterized using Powder X-ray diffraction, Field Emission Scanning Electron Microscopy, Electrical Resistivity, and Seebeck coefficients. The resulting materials showed a peak broadening from  $\text{Bi}_2\text{Te}_3$  to  $(\text{Bi}_{0.98}\text{Ge}_{0.02})_2\text{Te}_{2.7}\text{Se}_{0.3} / \text{Bi}_2\text{Te}_3$  20% due to the disorderedness in the crystal. Selenium atoms in  $\text{Bi}_2\text{Te}_3$  created donor-like voids in the lattice, leading to more porosity patches during sintering. The composites had higher intensity compared to the  $(\text{Bi}_{0.98}\text{Ge}_{0.02})_2\text{Te}_{2.7}\text{Se}_{0.3}$  sample. At a higher Ge doping concentration, wave functions of the Ge acceptors overlap, forming an impurity band. The Ge atoms function as acceptors in the  $\text{Bi}_2\text{Te}_3$  lattice through the substitution of Se on Te atoms, insertion of Ge into the Bi cation sublattice, and occupation of van der Waals gap sites through

**Table 4** Comparison of the present work with the other reported work

S. No	Author	Compound	PF ( $\mu\text{W}/\text{mK}^2$ )	Electrical resistivity $\rho(\Omega\text{m})$	Seebeck Coefficient $\mu\text{V}/\text{K}$	References
1	Junquin	$\text{Ge}_{1-x}\text{Pb}_x\text{Te}$	400	$1 \times 10^{-4}$	100	[38]
2	Chun Chun	$\text{Ga-Bi}_2\text{Te}_3$	0.416	$60 \times 10^{-4}$	50	[39]
3	Di Wu	$\text{GaTe}/\text{Bi}_2\text{Te}_3$	10	0.05	50	[40]
<b>4</b>	<b>Hegde, Prabhu</b>	<b><math>(\text{Bi}_{0.98}\text{Ge}_{0.02})_2\text{Te}_{2.7}\text{Se}_{0.3}</math></b>	<b>110</b>	<b><math>2 \times 10^{-4}</math></b>	<b>110</b>	<b>*Present work</b>

The bold script signifies the present research work’s Power factor, Electrical resistivity and Seebeck coefficient values.

defect engineering so the power factor value was enhanced by about 5.4 times in  $(\text{Bi}_{0.98}\text{Ge}_{0.02})_2\text{Te}_{2.7}\text{Se}_{0.3}$  compound to the pristine. This property makes the compound suitable for thermoelectric applications.

## Acknowledgements

Swaraangi Shirodkar would like to thank Manipal Academy of Higher Education for their financial support. A. N. Prabhu is grateful for the financial assistance granted by UGC-DAE, Mumbai (UDCSR/MUM/AU/CRS-M-314/204/298). The author, Ashok Rao, acknowledges that funds supplied under project number DST-FIST project (SR/FIST/PS-1/2017/8) were used to partially finish the research effort. One of the authors, Ganesh Shridhar Hegde, would like to thank REVA University for their support in this collaborative research project.

## Author contributions

Sample synthesis and preliminary analysis: Swaraangi Shirodkar. Methodology: Swaraangi Shirodkar and Suchitra Putran. Review and writing of research work: Swaraangi Shirodkar, A. N. Prabhu, Ashok Rao, and Ganesh Shridhar Hegde. Data curation and analysis: Swaraangi Shirodkar and Deepika Shanubhogue U.

## Funding

Open access funding provided by Manipal Academy of Higher Education, Manipal.

## Data availability

The thermoelectric data were collected at the Centre of Clean and Green Energy Centre, Department of Physics, Manipal Institute of Technology (MAHE), Manipal. The study's findings are accessible from the corresponding author [ANP] upon request.

## Declarations

**Competing interest** All authors certify that they have no links with or involvement in any organization or institution that has a financial or non-financial interest in the subject matter or materials covered in this manuscript.

**Ethical approval** The research leading to these results received partial funding from project grant (UDCSR/MUM/AU/CRS-M-314/204/298).

**Open Access** This article is licensed under a Creative Commons Attribution 4.0 International License, which permits use, sharing, adaptation, distribution and reproduction in any medium or format, as long as you give appropriate credit to the original author(s) and the source, provide a link to the Creative Commons licence, and indicate if changes were made. The images or other third party material in this article are included in the article's Creative Commons licence, unless indicated otherwise in a credit line to the material. If material is not included in the article's Creative Commons licence and your intended use is not permitted by statutory regulation or exceeds the permitted use, you will need to obtain permission directly from the copyright holder. To view a copy of this licence, visit <http://creativecommons.org/licenses/by/4.0/>.

## References

1. K. Kadel, L. Kumari, W.Z. Li, J.Y. Huang, P.P. Provencio, *Nanoscale Res. Lett.* **6**, 1–7 (2011)
2. G.S. Hegde, A.N. Prabhu, A. Rao, P.D. Babu, *Phys. B Condens. Matter.* **584**, 412087 (2020)
3. N.S. Abishek, K. Gopalakrishna Naik, *J. Cryst. Growth* **565**, 126141 (2021)
4. M.P. Lu, C.N. Liao, J.Y. Huang, H.C. Hsu, *Inorg. Chem.* **54**, 7438 (2015)
5. M. Noroozi, G. Jayakumar, K. Zahmatkesh, J. Lu et al., *J. Mater. Sci. Mater. Electron.* (2017). <https://doi.org/10.1149/2.0021710jss>
6. Y. Li, G. Wang, M. Akbari-Saatlu, M. Procek, H. Radamson, *Frontiers in Materials* **8**, 611078 (2021)
7. Z. Kong, G. Wang, R. Liang, J. Su, M. Xun, Y. Miao, H. Radamson, *H. Nanomaterials* **12**, 981 (2022)
8. Y. Miao, Y. Wang, H. Hu, X. Liu, H. Su, J. Zhang, H. Zhang, *Mater. Sci. Semicond. Process.* **85**, 134–140 (2018)

9. Y.H. Miao, H.Y. Hu, J.J. Song, R.X. Xuan, H.M. Zhang, *Chin. Phys. B* **26**(12), 127306 (2017)
10. N.K. Singh, J. Pandey, S. Acharya, A. Soni, *J. Alloy. Compd.* **746**, 350–355 (2018)
11. M.Y. Shtern, A.A. Sherchenkov, Y.I. Shtern, M.S. Rogachev, A.V. Babich, *NanoBiotechnology* **16**, 363–372 (2021)
12. C.H. Lin, W.T. Yen, Y.F. Tsai, H. Wu, *J. British J. Cancer* **3**(2), 1311–1318 (2020)
13. F. Wu, Q. He, M. Tang, H. Song, *Int. J. Mod. Phys. B* **32**(10), 1850123 (2018)
14. Z. Zhang, Y. Cao, Q. Tao, Y. Yan, X. Su, X. Tang, *J. Solid State Chem.* **292**, 121722 (2020)
15. H.H. Radamson, A. Hallén, I. Sychugov, A. Azarov, *Analytical methods and instruments for micro-and nanomaterials* (Springer, Berlin, 2023)
16. Z. Wang, V. Leonov, P. Fiorini, C. Van Hoof, *Sensors Actuators A Phys.* **156**, 95 (2009)
17. G.S. Hegde, A.N. Prabhu, A. Rao, M.K. Chattopadhyay, *Mater. Sci. Semicond. Process.* **127**, 105645 (2021)
18. A.M. Adam, E.M.M. Ibrahim, A. Panbude, K. Jayabal, P. Veluswamy, A.K. Diab, *J. Alloys Compd.* **872**, 159630 (2021)
19. S. Sumithra, N.J. Takas, D.K. Misra, W.M. Nolting, P.F.P. Poudeu, K.L. Stokes, *Adv. Energy Mater.* **1**, 1141 (2011)
20. G.S. Hegde, A.N. Prabhu, A. Rao, K. Gurukrishna, U. Deepika Shanubhogue, *J. Mater. Sci. Mater. Electron.* **33**, 25163 (2022)
21. G.S. Hegde, A.N. Prabhu, Y.H. Gao, Y.K. Kuo, V.R. Reddy, *J. Alloys Compd.* **866**, 158814 (2021)
22. M.K. Fuccillo, M.E. Charles, Y.S. Hor, S. Jia, R.J. Cava, *Solid State Commun.* **152**, 1208 (2012)
23. G.S. Hegde, V. Parol, A. Rao, A.N. Prabhu, J.J.B. Levinsky, G.R. Blake, *Mater. Res. Bull.* **145**, 111517 (2022)
24. B. Liang, Z. Song, M. Wang, L. Wang, W. Jiang, *J. Nanomater.* **2013**, 1 (2013)
25. K.-H. Kim, J.-H. Lee, Y.-K. Kyoung, S.-J. Choi, *Thin Solid Films* **524**, 157 (2012)
26. D. Liu, J. Stötzel, M. Seyring, M. Drüe, X. Li, R. Schmechel, M. Rettenmayr, *Cryst. Growth Des.* **16**, 617 (2016)
27. X.A. Fan, J.Y. Yang, W. Zhu, H.S. Yun, R.G. Chen, S.Q. Bao, X.K. Duan, *J. Alloys Compd.* **420**, 256 (2006)
28. R.O. Carlson, *J. Phys. Chem. Solids* **13**, 65 (1960)
29. J. Klikorka, M. Frumar, L. Tichý, L. Panák, H. Tichá, *J. Phys. Chem. Solids* **37**, 477 (1976)
30. Z. Liu, N. Sato, Q. Guo, W. Gao, T. Mori, *NPG Asia Mater.* **12**, 66 (2020)
31. P.J. Freud, G.M. Rothberg, *Phys. Rev.* **140**, A1007 (1965)
32. E. Tarnow, J.D. Joannopoulos, M.C. Payne, *Phys. Rev. B* **39**, 6017 (1989)
33. M.W. Oh, J.H. Son, B.S. Kim, S.D. Park, B.K. Min, H.W. Lee, *J. Appl. Phys.* (2014). <https://doi.org/10.1103/PhysRevB.39.6017>
34. S. Wang, W. Xie, H. Li, X. Tang, *Intermetallics* **19**, 1024 (2011)
35. G.S. Hegde, A.N. Prabhu, *J. Electron. Mater.* **51**, 2014 (2022)
36. A.H. Li, M. Shahbazi, S.H. Zhou, G.X. Wang, C. Zhang, P. Jood, G. Peleckis, Y. Du, Z.X. Cheng, X.L. Wang, Y.K. Kuo, *Thin Solid Films* **518**, 57 (2010)
37. Z. Zhang, Y. Cao, Q. Tao, Y. Yan, X. Su, X. Tang, *J. Solid State Chem.* **292**, 121722 (2020)
38. J. Li, C. Zhang, Y. Feng, C. Zhang, Y. Li, L. Hu, F. Liu, *J. Alloy. Compd.* **808**, 151747 (2019)
39. C.H. Lin, W.T. Yen, Y.F. Tsai, H.J. Wu, *ACS Appl. Energy Mater.* **3**(2), 1311–1318 (2020)
40. D. Wu, L.D. Zhao, S. Hao, Q. Jiang, F. Zheng, J.W. Doak, J. He, *Joule* **36**(32), 11412–11419 (2014)

**Publisher's Note** Springer Nature remains neutral with regard to jurisdictional claims in published maps and institutional affiliations.